Supporting Information

Reversibly tuning thermopower enabled by phase-change electrolyte for low-grade heat harvesting

Yinghong Xu[1], Zhiwei Li[1], Simin Li, Shengliang Zhang, Xiaogang Zhang[*]

Jiangsu Key Laboratory of Electrochemical Energy Storage Technologies, College of Material Science and Technology, Nanjing University of Aeronautics and Astronautics, Nanjing 211106, China

[*]Correspondence to X. Z. (azhangxg@nuaa.edu.cn)

[1] These authors contributed equally to this work.

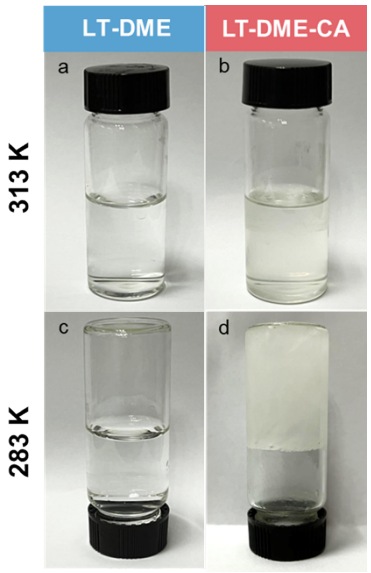

Figure S1. The digital photograph of designed electrolyte under different temperature. (a) and (c) The LT-DME electrolyte under 313 K and 283 K, respectively. (b) and (d) The LT-DME-CA electrolyte under 313 K and 283 K, respectively.

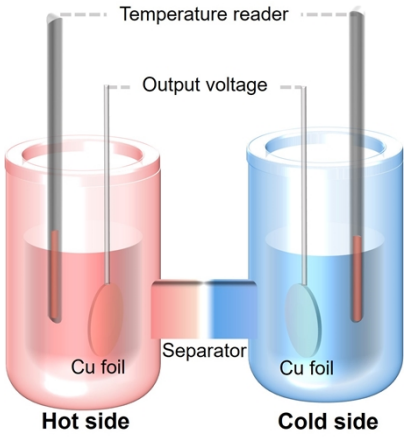

Figure S2. The non-isothermal H cell with symmetrical copper foils as electrodes was used to measure the performance of the designed electrolyte. The temperature on the hot and cold sides is controlled by thermostatic baths.

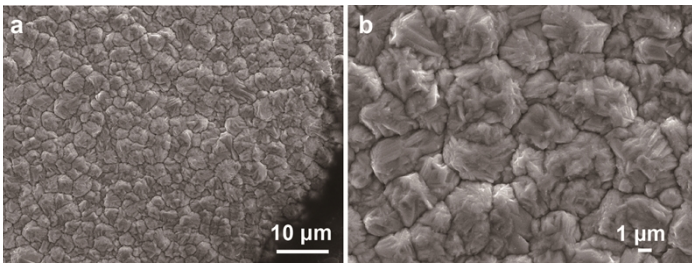

Figure S3. (a) and (b) The surface morphology images of Cu foil under different magnifications.

The morphology of Cu foil exhibits a microparticle structure with a similar planar. The rough surface promotes electrodes with a higher contact area for storing ions.

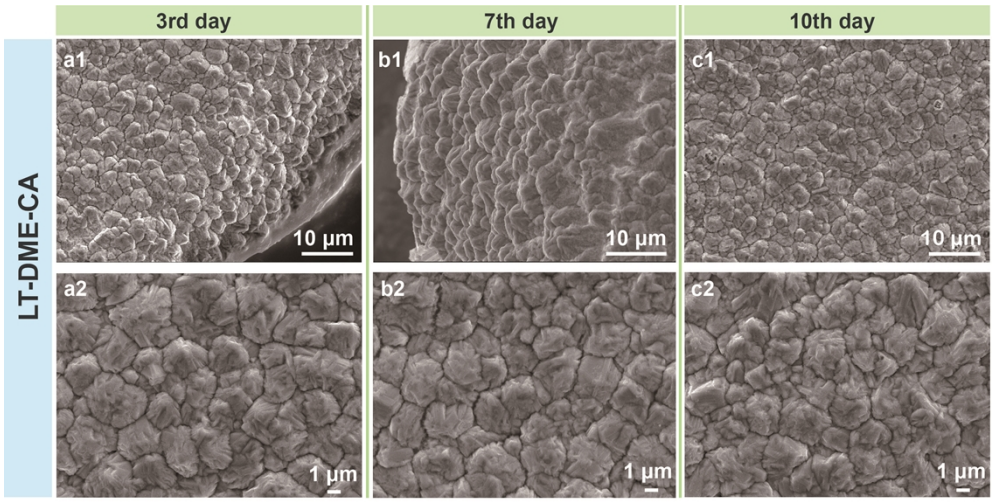

Figure S4. Morphology changes of Cu foil in LT-DME-CA electrolyte with soaking (a1, a2) 3 days, (b1, b2) 7 days, and (c1, c2) 10 days.

The morphology of Cu electrodes after immersing in LT-DME-CA electrolytes for different times was detected by SEM. When comparing with the morphology of pristine Cu foil in Fig. S3, the Cu electrode in LT-DME-CA shows a flat surface with similar intact microparticle morphology (Fig. S4a1-a2 and b1-b2) and no obvious defects at the edges. As depicted in Fig. S4c1 and c2, the surface remains stable without serious byproducts or uneven defects even after 10 days, indicating the good stability of Cu electrode in LT-DME-CA. In other words, the contribution on the thermoelectrochemical performances (voltage and current) induced by the possible corrosion of Cu electrode in LT-DME-CA electrolyte is negligible.

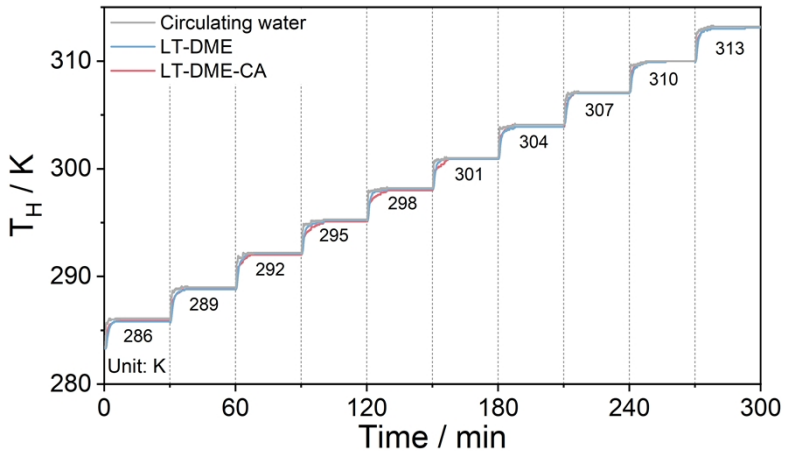

Figure S5. Absolute temperature of hot side for LT-DME and LT-DME-CA based TECs and circulating water in temperature controller.

The circulating water can reach the set temperature within tens of seconds and subsequently stabilize during the heating process. LT-DME and LT-DME-CA electrolytes require more time (few minutes) to achieve a steady state. Interestingly, the LT-DME-CA needs a longer time to reach equilibrium compared to LT-DME when situated near the phase transition temperature (295 ~ 301 K). Such phenomenon may be attributed to the heat absorption required by LT-DME-CA to overcome the intermolecular forces between DDCA molecules during the melting process, thereby facilitating the phase transition. Worthily, this melting process does not affect the overall temperature of the LT-DME-CA during the thermoelectrochemical tests.

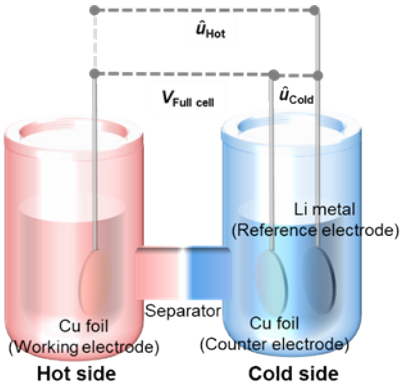

Figure S6. Schematic of non-isothermal three-electrode setup**.**

The non-isothermal three-electrode system used symmetrical copper foils as working and counter electrodes in both chambers. Because of the stable potential of the Li electrode, Li metal was selected as the reference electrode on the cold side. And the relationship between the potential of the cold electrode and the hot electrode and the voltage of the full cell can be written as:

$V_{Full\ cell} = E_{Hot} - E_{Cold}$

where the E_{Hot} and E_{Cold} are the potential of working electrode (electrode at hot side) and counter electrode (electrode at cold side) versus reference electrode (vs. Li/Li^+), respectively. And the $V_{Full\ cell}$ represents the voltage of full cell.

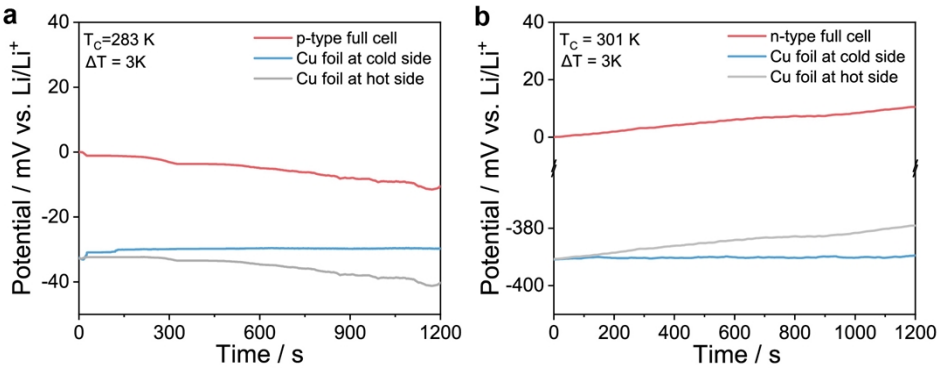

Figure S7. Recorded open-circuit voltage of the non-isothermal three-electrode setup using LT-DME-CA electrolyte. The real-time investigation of potential for each electrode and the voltage of full cell for (a) p-type and (b) n-type TECs.

The potential changes of each electrode were monitored via a non-isothermal three-electrode configuration as shown in Fig. S7a and b. Fig. S7a exhibits the open-circuit voltage of p-type TEC and the potential of each electrode during the thermal charging process. Clearly, the potential of Cu electrodes on the hot and cold sides gradually decreases and increases with the establishment of a temperature field, respectively, corresponding to the results of decreasing and increasing concentrations of Li^+ on the surface of Cu electrodes. Thus, an electric field that pointed from the electrode on the cold side to the electrode on the hot side was generated, which produced a negative thermovoltage ($V_{Full\ cell}=E_{Hot} - E_{Cold} < 0$). For the n-type full cell, the overall trend of potential is opposite to the p-type (Fig. S7b).

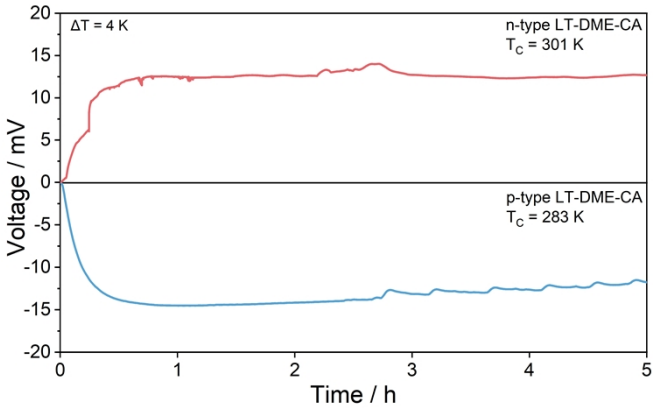

Figure S8. Durability of LT-DME-CA based TECs under ΔT=4 K.

The durability of both n-type and p-type TECs with the LT-DME-CA electrolyte is measured over 5 hours as shown in Fig. S8, and the temperature of the cold electrode for p-type TECs is set at 283 K. As shown in Fig. 2a, the LT-DME-CA based TEC switches from p-type to n-type when the temperature of the hot electrode is above the transition temperature of 301 K. Accordingly, the temperature of the cold electrode for the n-type TECs is fixed at 301 K to take full advantage of the n-type thermovoltage.

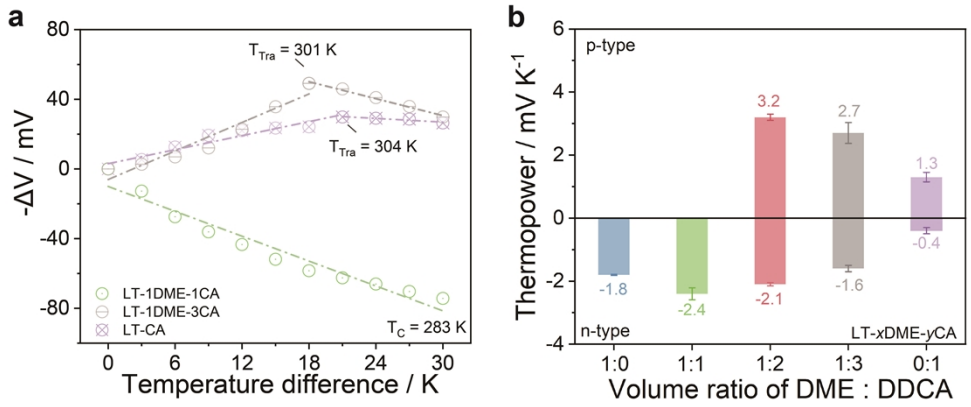

Figure S9. (a) The fitting curves of -ΔV versus ΔT for LT-1DME-1CA, LT-1DME-3CA, and LT-CA. (b) Thermopowers of LT-*x*DME-*y*CA.

To comprehensively study the influence of DDCA on tunning thermopower, a series of volume ratios between DME and DDCA, ranging from 1:1 to 1:3, were investigated and denoted as LT-*x*DME-*y*CA, where *x*:*y* represents the volume ratio of DME and DDCA. For convenience, we have labeled LT-1DME-2CA as LT-DME-CA in the manuscript. Fig. S9a shows that the LT-1DME-1CA based TECs have an n-type thermopower of -2.4 mV K^{-1}, indicating that a lower addition of DDCA results in the decrease of the phase change point and requires more energy to trigger the phase transition. When the volume ratio of DME:DDCA is adjusted to 1:3, LT-1DME-3CA based TECs enables the reversible polarization from p-type (2.7 mV K^{-1}) to n-type (-1.6 mV K^{-1}). For LT-CA, the switching trend of thermopower for LT-CA based TEC was similar to that for LT-1DME-3CA based TEC with higher phase transition temperature of 304 K. Combining the results of LT-DME and LT-1DME-2CA, the thermopower can achieve p-type switches to n-type above the transition temperature when the volume ratio between DME and DDCA exceeded the critical point of 1:1. It worth noting that the DME domains with higher Li salt concentration and CIP/AGG solvation structure are crucial for realizing fast Li^+ transportation in crystallized-state LT-1DME-*y*CA. However, as the volume ratio of DDCA increases (DME:DDCA=1:3), the crystallinity of the electrolyte is enhanced below the phase-change temperature. This increase in crystallinity impedes Li^+ transport, resulting in lower thermopower compared to p-type LT-1DME-2CA-based TECs. A poor p-type thermopower is displayed by the LT-CA for the same reason. In the liquid state, the Li^+ solvation

structure in the LT-DME electrolyte exists as an SSIP structure, and its diffusion mechanism is similar to that of the LT-1DME-*y*CA electrolytes in the liquid state. However, the Li^+ solvation structure of LT-1DME-*y*CA incorporates the long-chain DDCA molecule, which increases the size of the Li^+ solvation shell and hinders its transport. This results in an enlarged migration difference between cations and anions, leading to a higher n-type thermopower compared to LT-DME. The decrease in the n-type thermopower of LT-1DME-3CA and LT-CA may be related to the decline in ionic conductivity with the increase in the volume ratio of DDCA.

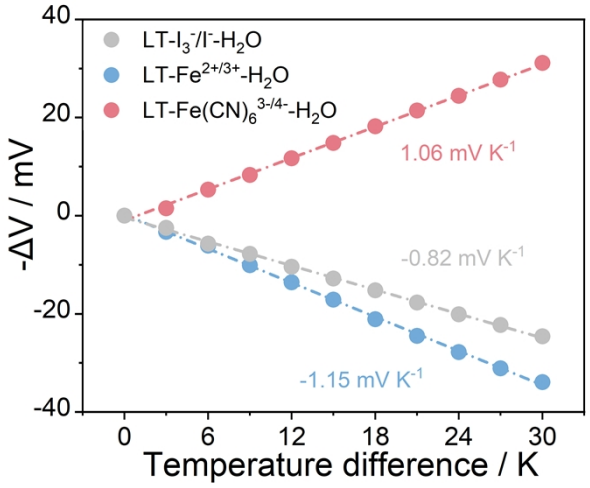

Figure S10. The fitting curves of -ΔV versus ΔT for LT-$Fe^{2+/3+}$-H_2O, LT-$Fe(CN)_6^{3-/4-}$-H_2O and LT-I_3^-/I^--H_2O based TECs.

The thermopower of the most common n-type or p-type redox couples (such as $Fe^{2+/3+}$, $Fe(CN)_6^{3-/4-}$, I_3^-/I^-) has been measured in the LT-H_2O system for comparison (Fig. S10). For the TECs based on the thermodiffusion effect and thermogalvanic effect, total S_i can be expressed as:

$$S_i = -\alpha_R + s_{td}(redox\ couple) + s_{td}(LT)$$

where the α_R is the temperature coefficient of the redox reaction ($O + ne \leftrightarrow R$), s_{td} represent the thermodiffusive thermopower.

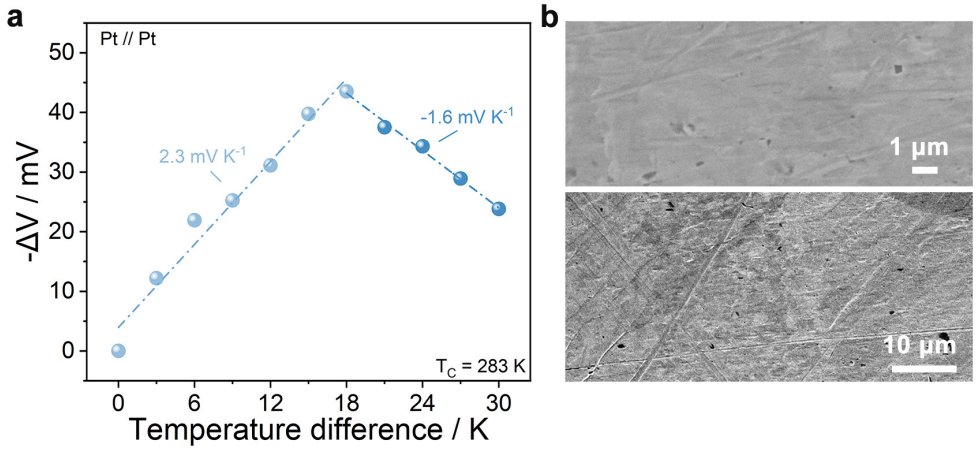

Figure S11. (a) The fitting curves of the -ΔV corresponding to related temperature differences for LT-DME-CA based TECs using symmetrical Pt electrodes system. (b) SEM images of Pt electrode under different magnifications.

As shown in Fig. S11b, the relatively smooth surface of Pt electrode means that the number of ions adsorbed during the thermoelectrochemical measurement is less than that of Cu electrodes. Thus, there are slight differences in the thermoelectrochemical performances by using different electrodes.

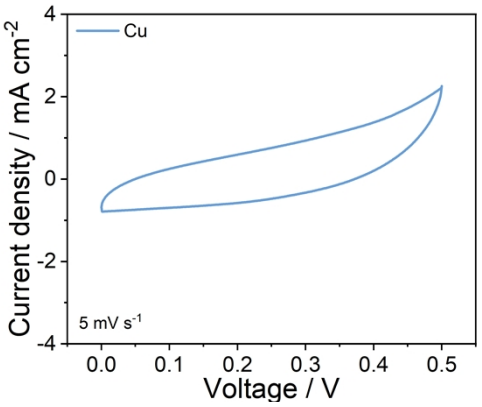

Figure S12. The electrochemical storage behavior of LT-DME-CA based TEC.

The CV curve exhibits a rectangular shape, which is comparable to the ideal behavior of an electric double-layer capacitor. This implies that the charge storage mechanisms of the LT-DME-CA based TECs are the consequence of the reversible adsorption of Li^+ and $TFSI^-$ onto the surface of Cu foil at the electrolyte/electrode interface.

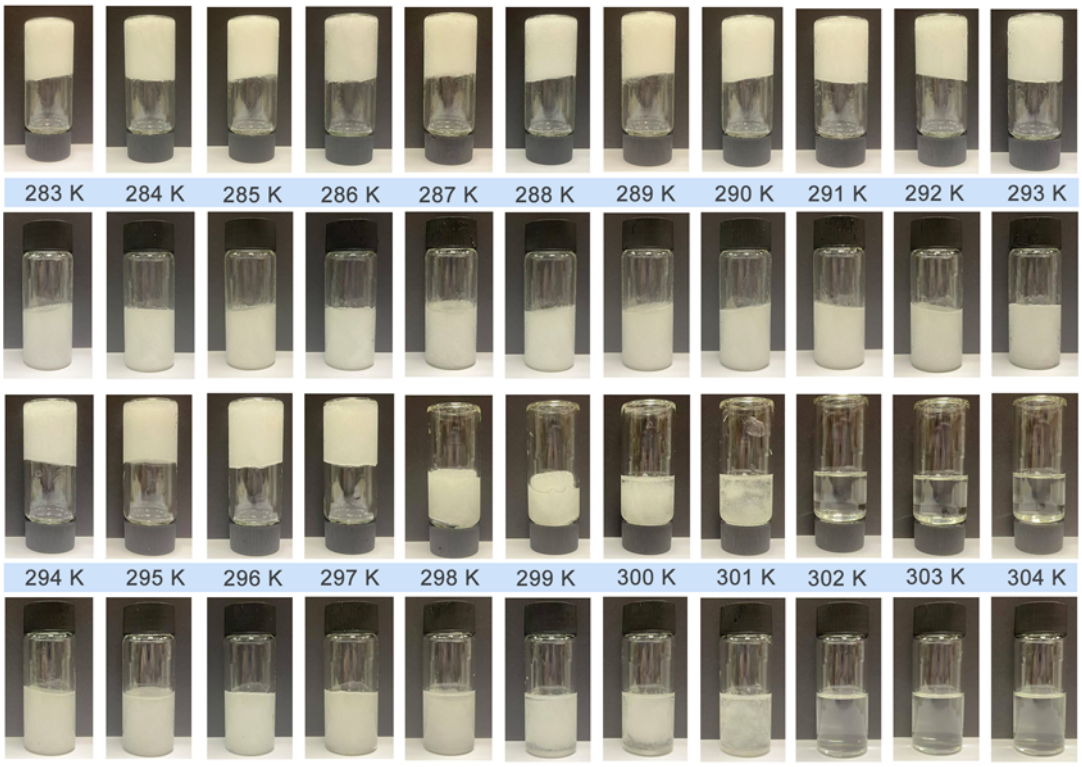

Figure S13. The photographs of LT-DME-CA after standing at different temperatures.

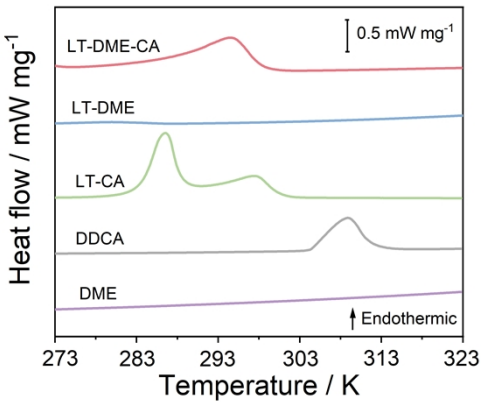

Figure S14. The DSC results of solvent and designed electrolyte.

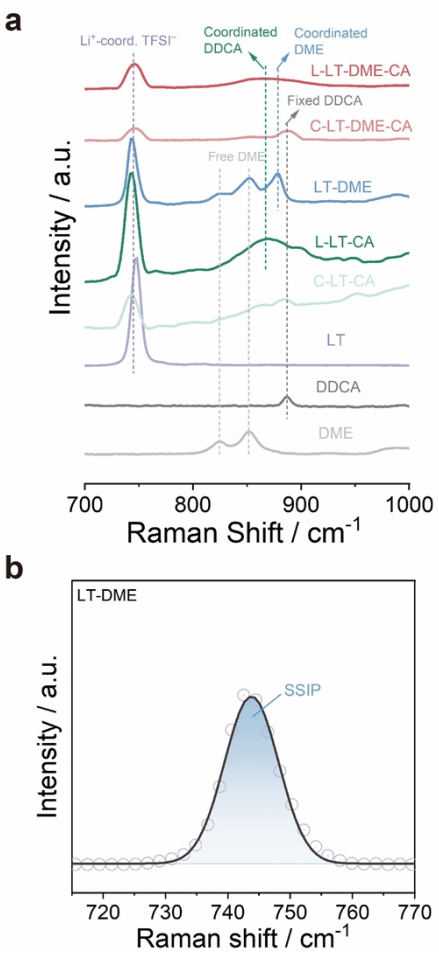

Figure S15. (a) The Raman spectra of lithium salt, solvent, and designed electrolyte. (b) The typical curve-fitting results of Raman spectroscopy for $TFSI^-$ coordination in LT-DME electrolyte.

The characterization of lithium salt and solvents were all conducted at 298 K. It worth noting that the DDCA solvent exist in the crystallized state when the temperature lower than about 304 K. In DDCA solvent, a typical peak at 887 cm^{-1} can be assigned to O−C−O bending. And this distinct peak at 887 cm^{-1} can also be observed in crystallized LT-CA (C-LT-CA) electrolyte, demonstrating the scattering model of frozen DDCA molecules. This peak in the LT-CA electrolyte with the liquid state (L-LT-CA) has a red shift to about 868 cm^{-1}, corresponding to Li^+-DDCA coordinated mode.

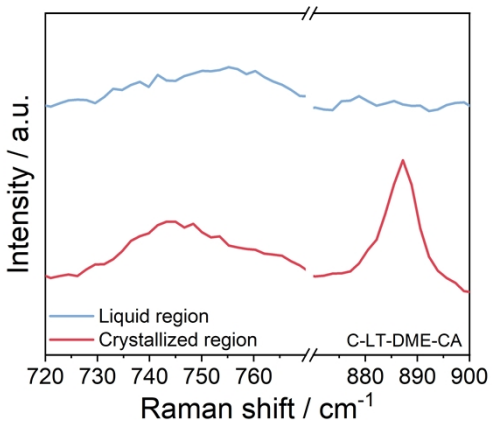

Figure S16. The Raman spectra correspond to the Raman mapping of the liquid and crystallized regions in C-LT-DME-CA.

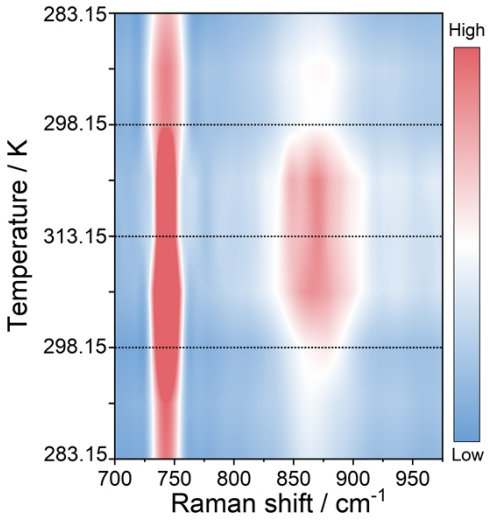

Figure S17. Contour map of variable-temperature Raman spectroscopy for LT-DME-CA electrolyte.

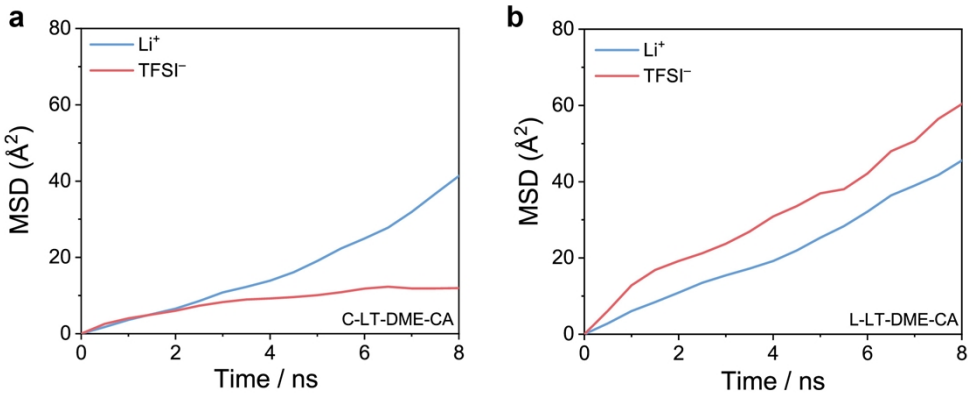

Figure S18. The calculated mean square displacement (MSD) of Li^+ and $TFSI^-$ ions in (a) C-LT-DME-CA and (b) L-LT-DME-CA electrolyte as a function of the simulation time.

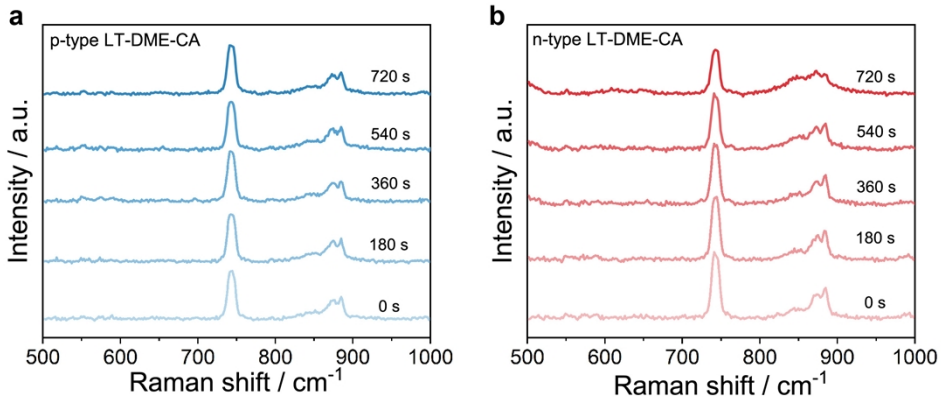

Figure S19. *In situ* line-scanning Raman analysis to monitor real-time concentration changes of $TFSI^-$ in LT-DME-CA based TEC. (a) p-type and (b) n-type LT-DME-CA based TEC at electrode and electrolyte interfaces in the range of 500-1000 cm^{-1}.

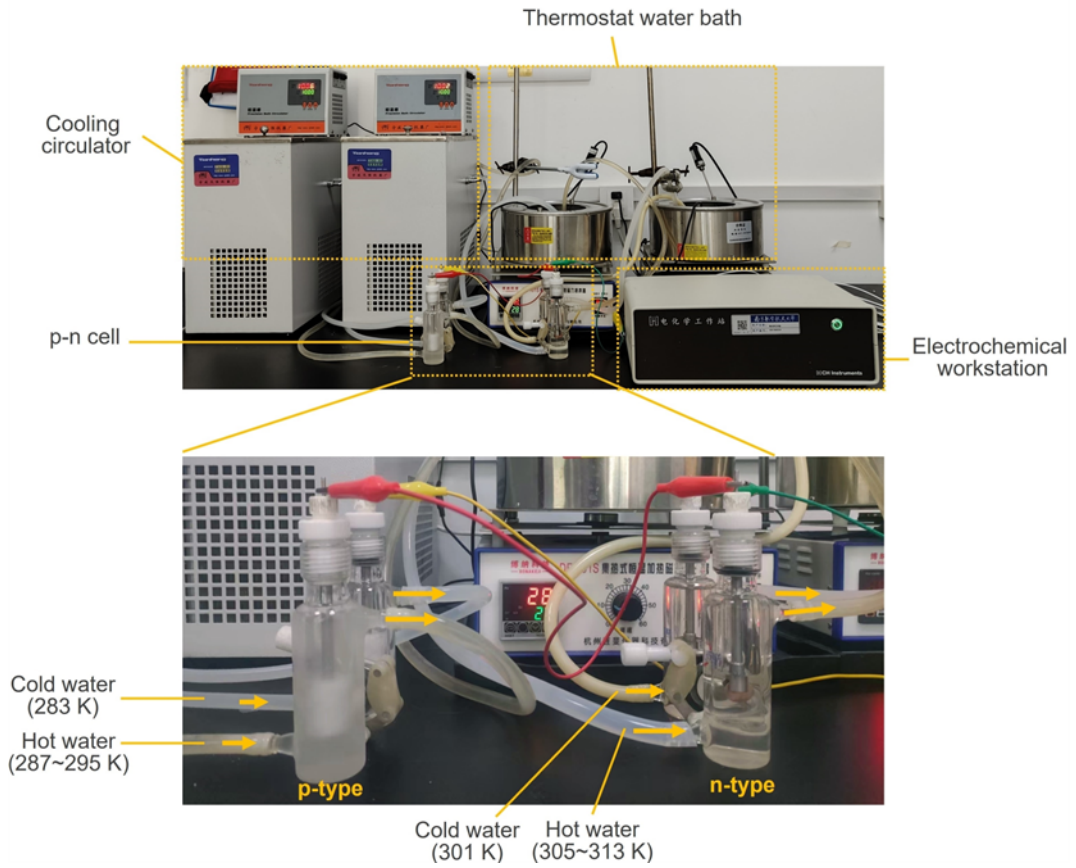

Figure S20. Digital photo of test equipment for p-n TECs using the LT-DME-CA electrolyte.

During the measurements, the hot side of the p-type TECs is heated by a cooling circulator (Ningbo Tianheng Instrument Factory, THD-05), while the cold side is kept at 283 K to establish a stable temperature difference. For the n-type TECs, the hot side is controlled by a hot water bath (BONAKEJI, DF-101S), and the cold side is maintained at 301 K. Moreover, the open-circuit voltage of p-n system is recorded by the electrochemical working station (CHI 760E).

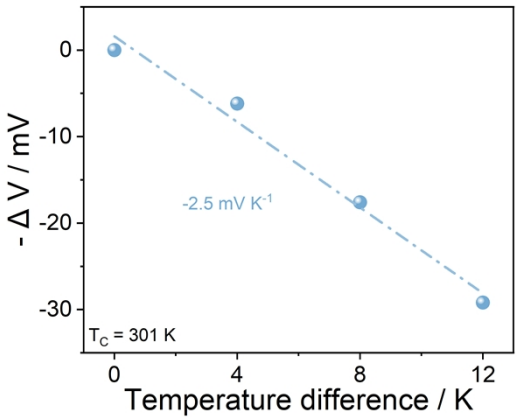

Figure S21. The fitting results of voltage difference versus different values of ΔT for n-type TECs based on LT-DME-CA electrolyte.

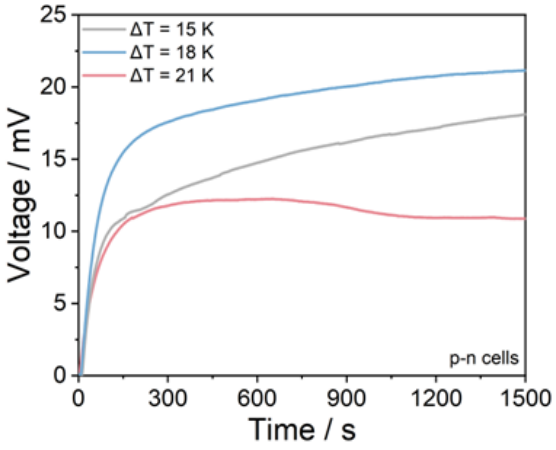

Figure S22. The output voltage of p-n TECs (n-type: T_C=301 K and T_H=313 K; p-type: T_C=283 K and T_H=298, 301, 304 K)

We have constructed independent p-type and n-type pouch cells connected in series and compared the voltage curves generated by p-n cells. It should point that the temperature difference of the p-type unit (T_C=283 K) was 15, 18, and 21 K, while keeping the hot and cold sides of the n-type component at 313 K and 301 K, respectively. This comparison aims to evaluate the effect of electrolyte phase transition on p-n TEC voltage. As shown in Fig. S22, an obvious decrease in output voltage for p-n TECs can be observed when temperature difference of p-type TECs beyond 18 K. This decline can be attributed to the conflict process between the voltage generated by the n-type transformation from p-type TECs and the voltage generated by the n-type component itself.

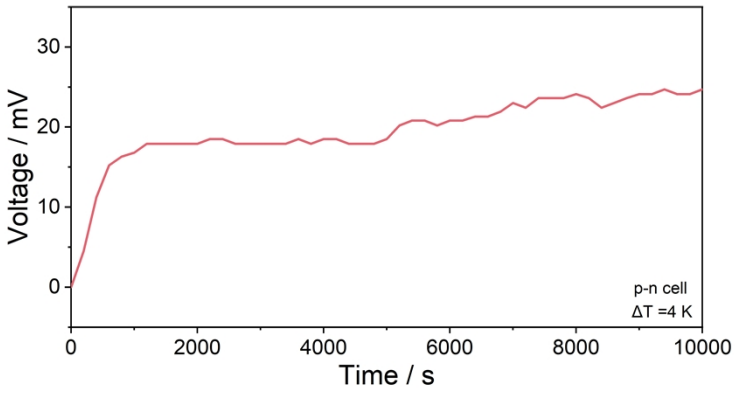

Figure S23. Durability of LT-DME-CA based p-n TECs within 10000 s.

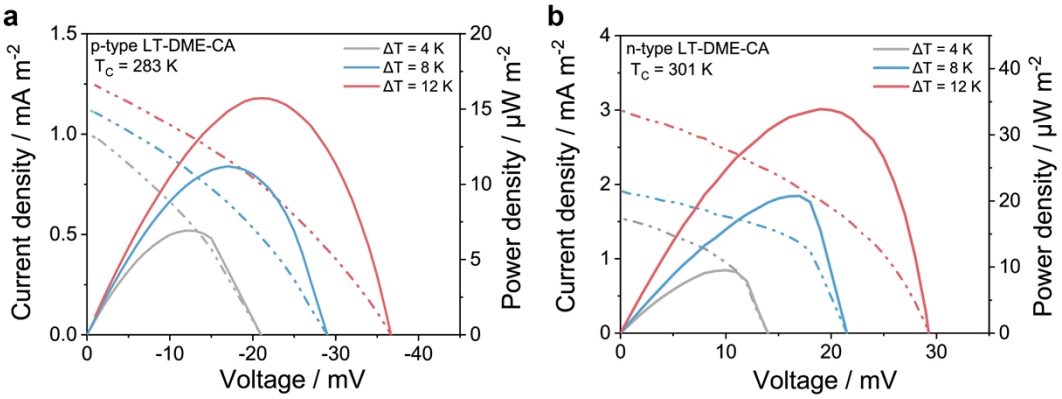

Figure S24. The power generation performance of the LT-DME-CA based TECs. Current-voltage and power-voltage curves for (a) p-type and (b) n-type LT-DME-CA based TECs.

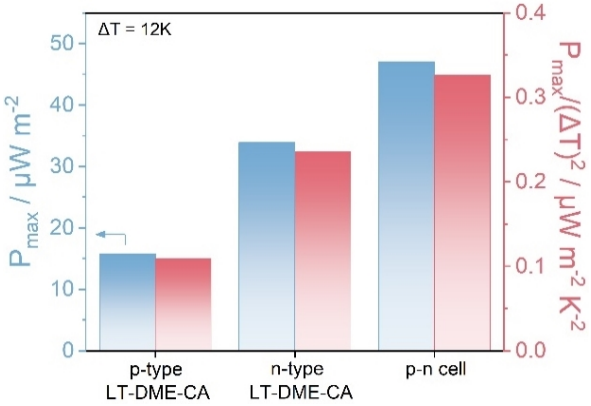

Figure S25. The maximum specific output power density and the corresponding normalized power density of p-type, n-type and p-n TECs based on LT-DME-CA electrolyte.

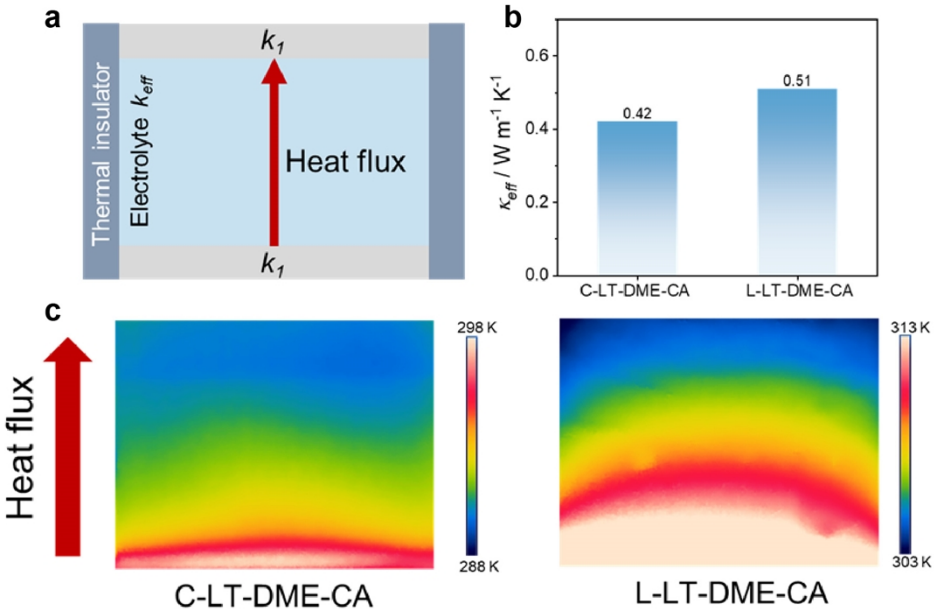

Figure S26. Thermal conductivity characterization of LT-DME-CA. (a) The illustration of thermal conductivity measurement by steady-state method. (b) The thermal conductivity of C-LT-DME-CA and L-LT-DME-CA, and the corresponding (c) temperature distribution across the whole cell was photographed by infrared camera. The thermal conductivity of the copper foil used is 403.20 W $m^{-1} \cdot K^{-1}$ based on laser flash technique (NETZSCH LFA-467).

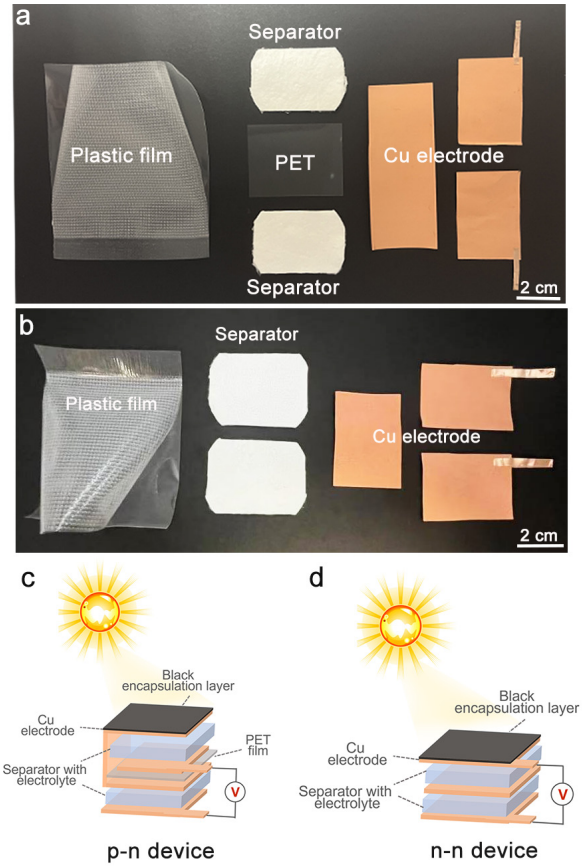

Figure S27. (a) Pouch cell configuration of p-n TECs using the LT-DME-CA electrolyte and (c) the corresponding illustration of p-n type stacked structure. (b) Pouch cell configuration of n-n TECs using the LT-DME electrolyte and (d) the corresponding illustration of n-n type stacked structure.

The p-n device using the LT-DME-CA electrolyte includes Cu electrodes, PET film, and glass microfiber separators (Fig. S27a). Before sealed with the plastic film, the separators are immersed with the electrolyte. Here, a black encapsulation layer (BEL) serves as the radiative heating layer, absorbing light and converting it to heat energy, which naturally generates a ΔT between BEL and back of p-n device that enables heat-to-energy conversion. Meanwhile, the other types of n-n devices are fabricated based on the LT-DME electrolyte. A n-n device consists of two n-type LT-DME TECs. The stacking forms of n-n device is quite different from p-n TECs as shown in Fig. S27d.

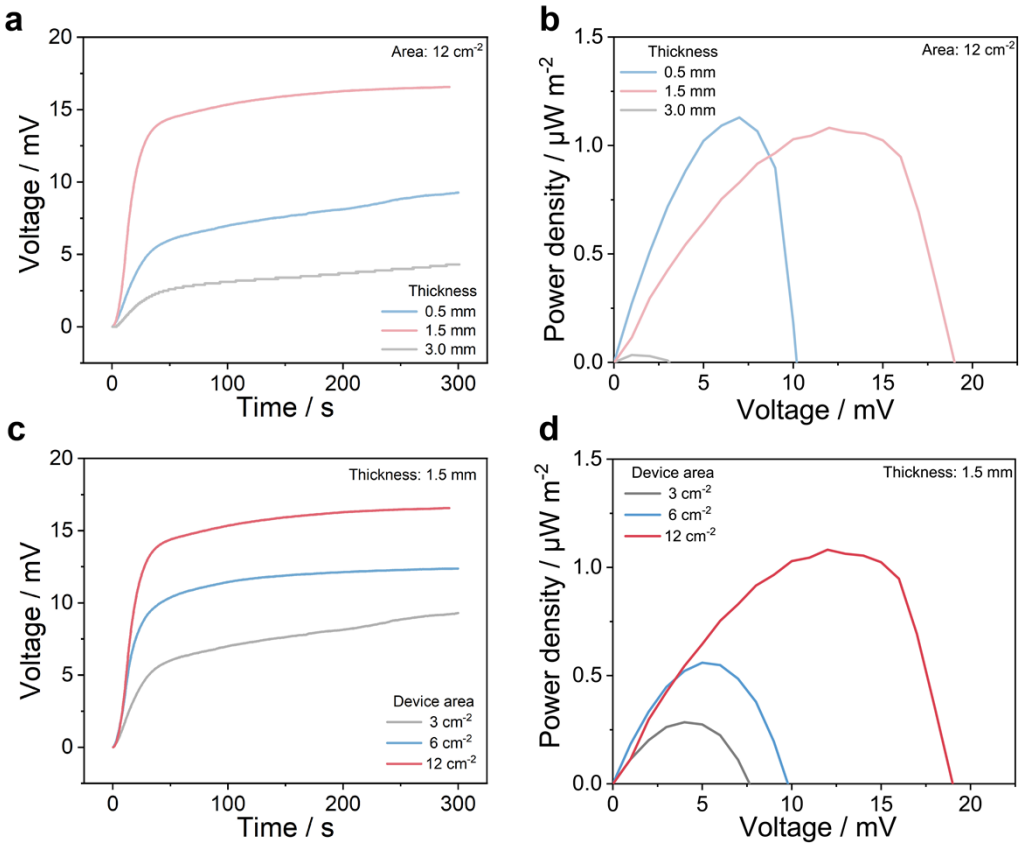

Figure S28. (a) Output voltage and (b) power density of devices with different thickness. (c) Output voltage and (d) power density of devices with different areas.

The thickness and area of LT-DME-CA based p-n device was optimized using pouch cell, where the temperature of the hot side (309 K) and cold side (293 K) are controlled by commercial Peltier plates. Under a certain area of device (12 cm^2), the output voltage initially increases (from 9.2 mV to 16.6 mV) with thickness (from 0.5 mm to 1.5 mm) and then decreases (4.3 mV with a thickness of 3.0 mm) (Fig. S28a). This trend may be related to the decrease of ionic transport kinetics as thickness increases. Therefore, the output power decreases significantly (from ~1.1 μW m^{-2} to 0.034 μW m^{-2}) when the thickness increases from 0.5 mm to 3.0 mm, as depicted in Fig. S28b. It is worth mentioning that the output voltage of TECs increases with an expansion in device area, as a larger device area accommodates more electrolyte ions (Fig. S28c). Correspondingly, the output power reaches the maximum value (~1.1 μW m^{-2}) when the area is 12 cm^2 (Fig. S28d).

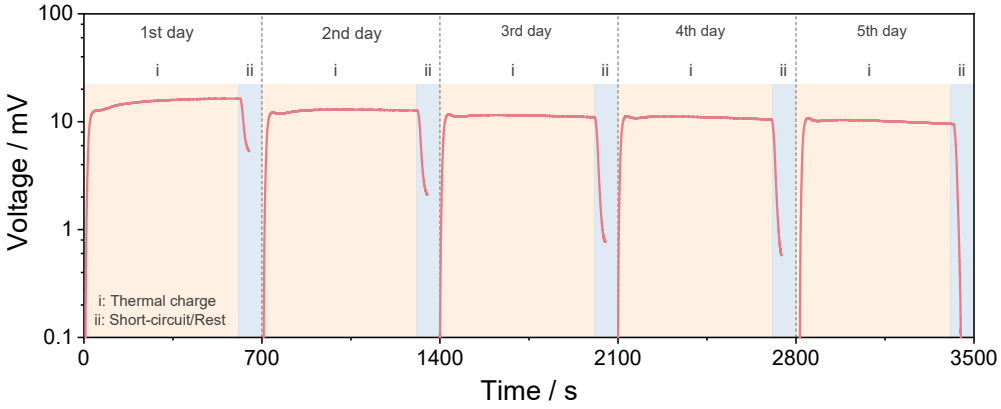

Figure S29. The voltage built-up stage of LT-DME-CA based p-n device under light on in various days (Solar intensity 1 kW m^{-2}).

The long-time power generation of LT-DME-CA based p-n device was tested in a pouch cell over five days, which went through three stages in one day: voltage build-up (thermal charge for ~600 s) under light on with the solar intensity 1 kW m^{-2} (the corresponding temperature of ~311 K for the BEL and ~293 K for the CS). After measurement, two electrodes of device were directly connected in a short-circuit with the light off (ΔT = 0 K, ~4 h) that ensure the open-circuit voltage returned to zero, and then rested until the next day's test.

Table S1. Comparison of the thermopower with reported in the literature for Figure 2c.

Label name	Electrolyte	Electrode	Absolute Thermopower	Ref.
This work	LT-DME-CA	Cu//Cu	2.1 mV K^{-1} n-type	/
			3.2 mV K^{-1} p-type	/
This work	LT-$Fe(CN)_6^{4-/3-}$-H_2O	SS//SS	1.06 mV K^{-1}	/
Lei et al.	$Fe(CN)_6^{4-/3-}$NaCl solution-P(AM-co-AMPS)	Pt//Pt	1.6 mV K^{-1}	*Joule* **5**, 2211-2222 (2021).
Shi et al.	$Fe(CN)_6^{4-/3-}$-NaCl solution-PNAGA-F68	Pt//Pt	2.17 mV K^{-1}	*Adv. Funct. Mater.* **33**, 2211720 (2023).
Lu et al.	$Fe(CN)_6^{4-/3-}$-gelatin/betaine	CNTPs//CNTPs	2.2 mV K^{-1}	*Angew. Chem. Int. Ed.* e202405357 (2024).
This work	LT-$Fe^{2+/3+}$-H_2O	SS//SS	1.15 mV K^{-1}	/
Peng et al.	$Fe^{2+/3+}$-PAM	Pt//Pt	1.43 mV K^{-1}	*Nano-Micro Lett.* **14**, 81 (2022).
Ding et al.	$Fe^{2+/3+}$-PAM	PDMS/CNT//PDMS/CNT	1.05 mV K^{-1}	*Adv. Energy Mater.* **11**, 2102219 (2021).
Xu et al.	$Fe^{2+/3+}$-PVA	Graphite//Graphite	1.65 mV K^{-1}	*Adv. Energy Mater.* **12**, 2201542 (2022).
This work	LT-I_3^-/I^--H_2O	SS//SS	0.82 mV K^{-1}	/
Duan et al.	I_3^-/I^--H_2O	Graphite//Graphite	1.91 mV K^{-1}	*Nano Energy* **57**, 473-479 (2019).
Zhou et al.	I_3^-/I^--α-CD-H_2O	Pt//Pt	2.0 mV K^{-1}	*J. Am. Chem. Soc.* **138**, 10502-10507 (2016).

Table S2. Comparison of methods and parameters for reported p-n conversion in TECs.

Electrolyte	p-n conversion method	Reversibility	Phase transition temperature	p-type/n-type Thermopower	Ref.
PNIPAM-I^-/I_3^--H_2O (redox based TEC)	PNIPAM, with a low critical solution temperature, is hydrophilic at low temperatures and transforms into a hydrophobic state at higher temperatures, allowing I_3^- at the hot side to be captured by the dehydrated form.	Irreversible	/	0.71/-1.91 mV K^{-1}	*Nano Energy* **57**, 473-479 (2019).
PNIPAM-I^-/I_3^--SMARS-H_2O (redox based TEC)	The separable trapping and manipulation of the inherent hydrophobic I_3^- parts of I^- /I_3^- that yield a dynamic internal gradient by PNIPAM.	Irreversible	/	1.5/-1.4 mV K^{-1}	*Sci. Adv.* **7**, eabe3184 (2021).
Methylcellulose (MC)-I^-/I_3^--H_2O (redox based TEC)	Based on the temperature-dependence of MC, hydrophobic interaction exists between MC and I_3^- ions at high temperature.	Reversible	316 K	1.48/-1.32 mV K^{-1}	*Sci. Adv.* **8**, eabl5318 (2022).
PVDF-HFP /NaTFSI/PC/TPFPB (redox-free TEC)	Introducing negative-charged TPFPB	Irreversible	/	20/-6 mV K^{-1}	*Nat. Commun.*

	additives and adjusting their amounts.				**13**, 221 (2022).
LT-DME-CA (redox-free TEC)	Based on the phase-change of electrolyte, modulate the ion transport environment.	Reversible	301 K	3.2/-2.1 mV K^{-1}	This work

Table S3. Tentative band assignments of LT-DME-CA from 2Dcos.

Raman shift / cm^{-1}	**Tentative assignments**
742	SSIPs
747	CIPs
753	AGGs
868	Coordinated DDCA
876	Coordinated DME

Table S4. Signs of cross-peaks in synchronous spectrum.

	742	**747**	**753**	**868**	**876**
876	+	+	+	+	
868	+	+	+		
753	+	+			
747	+				
742					

Table S5. Signs of cross-peaks in asynchronous spectrum.

	742	**747**	**753**	**868**	**876**
876	-	-	+	-	
868	-	-	+		
753	-	-			
747	-				
742					

Table S6. Result of multiplication on the signs of each cross-peaks in synchronous and asynchronous spectrum.

	742	**747**	**753**	**868**	**876**
876	-	-	+	-	
868	-	-	+		
753	-	-			
747	-				
742					

Each positive value in the table represents a response in which the wave number on the horizontal axis is faster than that on the vertical axis, and each negative value reflects a response in which the wave number on the horizontal axis is slower than that on the vertical axis. Based on the above analysis, the final responsive order for LT-DME-CA electrolyte upon heating can be determined as 753→876→868→747→742 cm^{-1}.